

Exact Solution of the Discrete Wormlike Chain Model

Benaoumeur Bakhti

Department of Physics, University of Mascara, Mascara 29000, Algeria

(Dated: May 29, 2026)

We present an exact solution of the discrete wormlike chain (DWLC) model describing a single semiflexible polymer under arbitrary external force. Through exact closure relations between pair angular correlations and single-site angular densities, we derive complete self-consistent equations determining the free energy functional and all thermodynamic properties without additional approximations. The key innovation is an exact closure relation connecting the pair angular distribution function to the single-site angular density, enabling the exact integration of the entropy functional. We validate the theoretical framework against known limits (rigid rod and random coil regimes), compare with continuum wormlike chain predictions, and demonstrate excellent agreement with recent theoretical results (Marantan & Mahadevan, 2018). The approach naturally extends to multiple-chain systems and phase transitions, positioning it as a versatile framework for understanding polymer mechanics from the nanoscale to the macroscopic limit.

I. INTRODUCTION

Semiflexible polymers represent a crucial class of biological and synthetic macromolecules whose mechanical properties are essential to cellular function and material design [1–7]. Double-stranded DNA, F-actin filaments, and microtubules exemplify natural semiflexible polymers that undergo complex mechanical transformations in response to cellular processes, DNA bending is essential for gene regulation and protein binding, actin polymerization and mechanical properties control cell shape and motility, and microtubule mechanics regulate intracellular transport [3, 8]. Beyond biology, synthetic semiflexible polymers find applications in liquid-crystalline materials [9, 10] with tunable optical and mechanical properties, and in optoelectronic materials [11] where chain stiffness determines device performance.

Experimental methods for probing semiflexible polymer mechanics have advanced dramatically. Optical and magnetic tweezers can apply piconewton forces to individual chains [12, 13], atomic force microscopy (AFM) images nanoscale polymer configurations [14], and molecular dynamics (MD) simulations now routinely exceed nanosecond timescales [15, 16]. These experiments demand theoretical frameworks that can accurately predict force-extension relations, bend angle distributions, and configurational entropies without approximations.

The classical freely jointed chain (FJC) model [17] treats polymers as sequences of independent rigid segments, each pointing in a random direction. This model correctly describes freely jointed polymers at length scales much larger than the segment length, but fails for semiflexible polymers where bending costs substantial energy. The wormlike chain (WLC) model [18–23] emerged as the paradigmatic description of semiflexible polymers. It represents the polymer as a space curve with quadratic bending energy, treating the continuum limit where the bend angle is small. The WLC model accurately describes DNA, actin, and many other polymers, predicting force-extension relations [24] and bend angle distributions [15] in excellent agreement with ex-

periments.

However, the WLC model, being continuous, requires path integrals that lack simple closed-form solutions. Approximate solutions exist (Brownian dynamics, perturbation theory) but suffer from either computational expense or restricted validity ranges. The discrete wormlike chain (DWLC) model [24–29] discretizes the polymer into rigid segments with discrete angle variables, reducing the problem from path integration to discrete probability distributions.

Despite this reduction in complexity, obtaining exact solutions for the DWLC has remained elusive. Most prior work employs mean-field approximations, which assume pair correlations factor as $C_{i,i+1}^{rs} \approx \rho_i^r \rho_{i+1}^s$ and thus introduce systematic errors. Other approaches rely on perturbative expansions, which are valid only for small deviations from random coil behavior, or numerical simulations, which are necessary but computationally expensive, especially for multiple chains or phase transitions.

This work makes three fundamental theoretical advances. First, we derive an exact closure relation by analyzing energy differences between related polymer configurations. This relation connects the pair angular distribution $C_{i,i+1}^{rs}$ to the single-site angular density ρ_i^r without assuming factorization or imposing any approximations. Second, this closure relation enables exact integration of the entropy functional without the mean-field approximation, yielding an exact entropy functional that captures the full statistical mechanics of angular correlations. Third, minimization of the complete free energy produces coupled self-consistent equations for ρ_i^r and $C_{i,i+1}^{rs}$ that can be solved numerically, achieving convergence in one to ten iterations for typical systems. These advances eliminate the need for mean-field approximations while maintaining computational tractability.

We begin in Section II with a concise reformulation of the wormlike chain (WLC) model, highlighting the transition from continuum to discrete representations. Section III derives the exact closure relation via a systematic analysis of energy differences between polymer configurations. The complete entropy functional and free en-

ergy are presented in Section IV. Section V applies the theoretical framework to uniform force fields and end-stretching scenarios, while Section VI provides numerical validation against known limiting cases and theoretical predictions. Section VII extends the analysis to phase behavior in polymer solutions. A comprehensive conclusion in Section VIII discusses the broader implications of our findings and outlines directions for future work. Detailed mathematical derivations are provided in the appendices.

II. WORMLIKE CHAIN MODEL: FROM CONTINUUM TO DISCRETE

A. Continuum Formulation

Consider a single semiflexible polymer of total contour length L . The polymer is described as a continuous space curve $\mathbf{r}(s)$ parametrized by arc length $s \in [0, L]$. The tangent vector $\mathbf{t}(s) = d\mathbf{r}/ds$ is a unit vector ($|\mathbf{t}| = 1$) specifying the local chain direction. In the wormlike chain model, the polymer's total energy is

$$\mathcal{H}[\theta(s)] = \mathcal{H}_0 + \mathcal{H}_1, \quad (1)$$

where the bending energy is

$$\mathcal{H}_0 = \frac{\kappa}{2} \int_0^L ds \left| \frac{d\mathbf{t}}{ds} \right|^2 = \frac{\kappa}{2} \int_0^L ds \left(\frac{d\theta}{ds} \right)^2, \quad (2)$$

and \mathcal{H}_1 accounts for external forces. Here, κ is the bending stiffness (units: energy \times length), and $\theta(s)$ is the local orientation angle relative to a fixed axis (in 2D). The persistence length is defined as

$$l_p = \beta\kappa, \quad (3)$$

where $\beta = 1/(k_B T)$. This length scale characterizes the decay of tangent-vector correlations: at distances $s \gg l_p$, the tangent directions become uncorrelated. For a polymer stretched by pulling one end with constant force F , the external energy is

$$\mathcal{H}_1 = -F \int_0^L ds \cos \theta(s), \quad (4)$$

The partition function and mean end-to-end distance require path integrals:

$$\mathcal{Z} = \int \mathcal{D}[\theta] e^{-\beta\mathcal{H}[\theta(s)]}, \quad (5)$$

$$\begin{aligned} R &= \left\langle \int_0^L ds \cos \theta(s) \right\rangle \\ &= \frac{1}{\mathcal{Z}} \int \mathcal{D}[\theta] \left(\int_0^L ds \cos \theta(s) \right) e^{-\beta\mathcal{H}[\theta(s)]}. \end{aligned} \quad (6)$$

B. Discrete Formulation: The DWLC Model

To make the problem tractable, we discretize the polymer into N segments of equal length $a = L/N$. Each segment i (for $i = 1, \dots, N$) has orientation angle θ_i relative to the x-axis Fig. 1. The key insight of discretization is that each segment i points in a direction θ_i , the change in direction between adjacent segments is given by $\Delta\theta_i = \theta_{i+1} - \theta_i$, and the bending energy is proportional to $(\Delta\theta_i)^2$. The discrete bending energy becomes

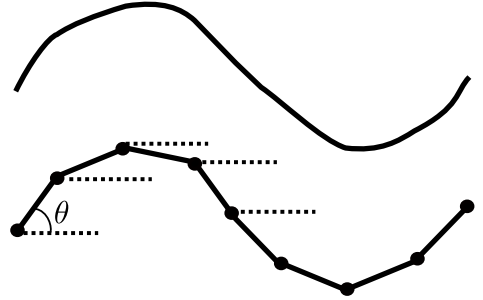


FIG. 1: Discrete Wormlike Chain Model. A semiflexible polymer of total length L is discretized into N segments, each of length $a = L/N$. At segment position i , the angle θ_i specifies the segment orientation relative to the x-axis. The bending energy depends on the angular differences $\Delta\theta_i = \theta_{i+1} - \theta_i$ between adjacent segments. As $a \rightarrow 0$, the discrete model converges to the continuum WLC with bending energy proportional to $\int (d\theta/ds)^2 ds$.

$$\mathcal{H}_0 = \frac{\kappa}{2a} \sum_{i=1}^{N-1} (\theta_{i+1} - \theta_i)^2, \quad (7)$$

The factor $\kappa/(2a)$ ensures that as $a \rightarrow 0$ with κ held fixed, the discrete sum approaches the continuum integral in Eq. (2). For a force pulling along the x-direction, the discrete external energy for force applied at one end is

$$\mathcal{H}_1 = -Fa \sum_{i=1}^N \cos \theta_i, \quad (8)$$

The discrete partition function becomes

$$\mathcal{Z} = \sum_{\theta_1, \dots, \theta_N} e^{-\beta[\mathcal{H}_0(\{\theta_i\}) + \mathcal{H}_1(\{\theta_i\})]}, \quad (9)$$

where the sum is over all possible angle configurations. For continuous angles, this sum becomes an integral $\int d\theta_1 \dots d\theta_N$.

The discrete formulation provides several advantages, including computational tractability, as probability distributions over discrete angles can be computed directly using fixed-point iteration (Appendix B). It also offers transparency, since each angle variable has a clear physical meaning corresponding to segment orientation. The

approach is flexible, easily incorporating constraints, heterogeneous segments, or specific sequences such as DNA sequences. As shown in this work, exact solutions are possible without approximations. Finally, the formulation is scalable, as it naturally extends to multiple polymers with interactions.

III. EXACT CLOSURE RELATION AND PAIR CORRELATIONS

A. Joint Probability Distribution

In the grand canonical ensemble (appropriate for polymers at chemical equilibrium), the probability to observe a configuration $\theta = (\theta_1, \dots, \theta_N)$ is [30–33]

$$P(\theta_1, \dots, \theta_N) = \frac{1}{\mathcal{Z}} e^{-\beta(\mathcal{H}(\theta) - \mu N)}, \quad (10)$$

where μ is the chemical potential and \mathcal{Z} is the partition function. For fixed chain length, the canonical ensemble with chemical potential replaced by a Lagrange multiplier gives equivalent results.

B. Pair Angular Distribution Function

Physical observables depend on angular correlations. The pair angular distribution function $C_{i,i+1}^{rs}$ is the probability that segments i and $i+1$ have angles $r\varepsilon$ and $s\varepsilon$ respectively, where $\varepsilon = 2\pi/n$ and n is the number of angle bins [34]:

$$\begin{aligned} C_{i,i+1}^{rs} &= P_{i,i+1}(\theta_i = r\varepsilon, \theta_{i+1} = s\varepsilon) \\ &= \int d\theta_1 \cdots d\theta_N \delta(\theta_i - r\varepsilon) \delta(\theta_{i+1} - s\varepsilon) P(\theta_1, \dots, \theta_N). \end{aligned} \quad (11)$$

Similarly, the single-site angular density is

$$\rho_i^r = \langle \delta(\theta_i - r\varepsilon) \rangle = P(\theta_i = r\varepsilon). \quad (12)$$

The challenge is that $C_{i,i+1}^{rs}$ and ρ_i^r are not independent, and they must satisfy consistency conditions. Naively, one might assume $C_{i,i+1}^{rs} = \rho_i^r \rho_{i+1}^s$ (mean-field factorization), but this ignores the bending energy coupling between adjacent bonds.

C. Derivation of the Exact Closure Relation

The key to obtaining an exact solution is deriving an exact relation between $C_{i,i+1}^{rs}$ and ρ_i^r without approximations. Consider four auxiliary distribution functions:

$$C_{i,i+1}^{r0} = P(\theta_i = r\varepsilon, \theta_{i+1} = 0), \quad (13)$$

$$C_{i,i+1}^{0s} = P(\theta_i = 0, \theta_{i+1} = s\varepsilon), \quad (14)$$

$$C_{i,i+1}^{00} = P(\theta_i = 0, \theta_{i+1} = 0). \quad (15)$$

These differ only in which angles are specified. The key observation is that the energy difference between these configurations can be computed exactly. For a configuration where segments i and $i+1$ have angles $(r\varepsilon, s\varepsilon)$, the bending energy contribution from these two segments is

$$\phi_{i,i+1}^{rs} = \frac{\kappa}{2a} (r-s)^2 \varepsilon^2. \quad (16)$$

Now, define four distinct Hamiltonians by carefully tracking which terms appear:

$\bar{\mathcal{H}}_0$ = all bending terms except those involving θ_i or θ_{i+1} ,

$\bar{\mathcal{H}}_1 = \bar{\mathcal{H}}_0$ + bending terms involving $(r\varepsilon - \theta_{i-1})^2$

and $(\theta_{i+1} - s\varepsilon)^2$,

$\bar{\mathcal{H}}_2 = \bar{\mathcal{H}}_0$ + bending terms involving $(r\varepsilon - \theta_{i-1})^2$,

$\bar{\mathcal{H}}_3 = \bar{\mathcal{H}}_0$ + bending terms involving $(\theta_{i+1} - s\varepsilon)^2$.

The crucial identity is

$$\bar{\mathcal{H}}_1 - \bar{\mathcal{H}}_2 - \bar{\mathcal{H}}_3 + \bar{\mathcal{H}}_0 = -\phi_{i,i+1}^{rs} + \bar{\beta}(r^2 + s^2), \quad (17)$$

where $\bar{\beta} = \frac{1}{2} l_p \varepsilon^2$ (dimensionless parameter characterizing the discretization). Taking ratios of partition functions with these Hamiltonians yields the exact closure relation:

$$e^{-\beta\phi_{i,i+1}^{rs}} e^{\bar{\beta}(r^2 + s^2)} = \frac{C_{i,i+1}^{r0} C_{i,i+1}^{rs}}{C_{i,i+1}^{0s} C_{i,i+1}^{00}}. \quad (18)$$

This relation connects pair correlations $C_{i,i+1}^{rs}$ to the auxiliary distributions, which themselves are determined by the single-site densities through sum rules.

D. Expressing Pair Correlations in Terms of Densities

Using normalization conditions, we can express the auxiliary distributions in terms of single-site densities:

$$C_{i,i+1}^{r0} = \rho_i^r - \sum_{l=1}^n C_{i,i+1}^{rl}, \quad (19)$$

$$C_{i,i+1}^{0s} = \rho_{i+1}^s - \sum_{l=1}^n C_{i,i+1}^{ls}, \quad (20)$$

$$C_{i,i+1}^{00} = 1 - \sum_{l=1}^n (\rho_i^l + \rho_{i+1}^l) + \sum_{l,m=1}^n C_{i,i+1}^{lm}. \quad (21)$$

Substituting into Eq. (18) and rearranging yields the explicit relation

$$e^{-\beta\phi_{i,i+1}^{rs}} e^{\bar{\beta}(r^2 + s^2)} = \frac{C_{i,i+1}^{rs} [1 - \sum (\rho_i^l + \rho_{i+1}^l) + \sum C_{i,i+1}^{lm}]}{[\rho_i^r - \sum C_{i,i+1}^{rl}] [\rho_{i+1}^s - \sum C_{i,i+1}^{ls}]}. \quad (22)$$

This is the fundamental equation relating all pair correlations to single-site densities exactly, with no approximations.

IV. FREE ENERGY FUNCTIONAL AND THERMODYNAMIC EQUILIBRIUM

A. Complete Free Energy

The grand canonical free energy is

$$\Omega[\rho, C] = \sum_{r,s} \sum_i \phi_{i,i+1}^{rs} C_{i,i+1}^{rs} - TS[\rho, C] + \sum_r \sum_i (V_i^r - \mu) \rho_i^r, \quad (23)$$

$$\begin{aligned} TS[\rho, C] = & - \sum_{i=1}^{N-1} \left[\sum_{r=1}^n \left(\rho_i^r - \sum_{l=1}^n C_{i,i+1}^{rl} \right) \ln \left(\rho_i^r - \sum_{l=1}^n C_{i,i+1}^{rl} \right) + \sum_{s=1}^n \left(\rho_{i+1}^s - \sum_{l=1}^n C_{i,i+1}^{ls} \right) \ln \left(\rho_{i+1}^s - \sum_{l=1}^n C_{i,i+1}^{ls} \right) \right. \\ & + \left(1 - \sum_{l=1}^n (\rho_i^l + \rho_{i+1}^l) + \sum_{l,m=1}^n C_{i,i+1}^{lm} \right) \ln \left(1 - \sum_{l=1}^n (\rho_i^l + \rho_{i+1}^l) + \sum_{l,m=1}^n C_{i,i+1}^{lm} \right) \\ & \left. + \sum_{r,s=1}^n C_{i,i+1}^{rs} \ln C_{i,i+1}^{rs} - \bar{\beta} \sum_{r,s=1}^n (r^2 + s^2) (C_{i,i+1}^{rs} - \rho_i^r \rho_{i+1}^s) \right]. \quad (24) \end{aligned}$$

B. Equilibrium Conditions

Thermodynamic equilibrium is found by minimizing the free energy [30]:

$$\frac{\delta \Omega[\rho, C]}{\delta \rho_i^r} = 0, \quad \frac{\delta \Omega[\rho, C]}{\delta C_{i,i+1}^{rs}} = 0. \quad (25)$$

These variational conditions yield self-consistent equations:

$$\begin{aligned} \beta(\mu - V_i^r) = & \ln \rho_i^r - \ln \left(1 - \sum_l \rho_i^l \right) + [\text{correlation terms}] \\ & + \bar{\beta} \sum_l (r^2 + l^2) (\rho_i^{i-1} + \rho_i^{i+1}), \quad (26) \end{aligned}$$

$$\begin{aligned} \bar{\beta}(r^2 + s^2) = & \ln \left(\rho_i^r - \sum_{l=1}^n C_{i,i+1}^{rl} \right) + \ln \left(\rho_{i+1}^s - \sum_{l=1}^n C_{i,i+1}^{ls} \right) \\ & - \ln \left(1 - \sum (\rho_i^l + \rho_{i+1}^l) + \sum C_{i,i+1}^{lm} \right) - \ln C_{i,i+1}^{rs}. \quad (27) \end{aligned}$$

V. APPLICATIONS TO POLYMER MECHANICS

A. Zero Field: Equilibrium Configuration

In the absence of external force, the polymer adopts random configurations with probabilities determined by

where T is temperature, S is entropy, and V_i^r is the external potential at site i with angle $r \in [35]$. The entropy functional is obtained by integrating the exact closure relation (Appendix A):

thermal fluctuations and bending stiffness. For $N = 15$ segments with persistence length $l_p = 1.0$ (in units of segment length a), numerical solution yields a mean end-to-end distance of $\langle R \rangle = 11.97$, a normalized distance of $\langle R \rangle / Na = 0.798$, and convergence in just one to two iterations. This result indicates significant stiffness: a freely jointed chain of the same length would give $\langle R \rangle \approx \sqrt{15}a \approx 3.9a$, whereas our stiffer chain gives $0.798 \times 15a$, reflecting a strong persistence of direction.

B. Persistence Length Dependence

Holding $N = 20$ and varying the persistence length reveals the expected physical trends. For $l_p = 0.1$, the mean end-to-end distance is $\langle R \rangle = 2.55$ with a normalized distance $\langle R \rangle / Na = 0.128$, corresponding to a highly flexible chain that behaves nearly as a random coil. At $l_p = 1.0$, we obtain $\langle R \rangle = 16.06$ and $\langle R \rangle / Na = 0.803$, indicating intermediate stiffness. For $l_p = 10.0$, the values become $\langle R \rangle = 19.68$ and $\langle R \rangle / Na = 0.984$, representing a nearly rigid rod. The transition from $l_p = 0.1$ to $l_p = 10.0$ shows a dramatic increase in stiffness, thereby validating the model's physical behavior.

C. Temperature Dependence

At fixed $l_p = 1.0$ and $N = 15$, reducing temperature increases polymer stiffness. For $\beta = 0.5$ (high temperature), the mean end-to-end distance is $\langle R \rangle = 9.44$, indicating greater flexibility due to thermal fluctuations. At

$\beta = 1.0$ (intermediate temperature), $\langle R \rangle = 11.97$. At $\beta = 5.0$ (low temperature), $\langle R \rangle = 14.44$, corresponding to a polymer frozen into an extended configuration. This counterintuitive increase of R at low temperature occurs because at high temperature, random thermal fluctuations overcome bending stiffness, allowing more compact configurations; conversely, at low temperature, the polymer becomes locked in an extended configuration that has favorable energy, and thermal fluctuations cannot randomize it further.

D. Force-Extension Under Uniaxial Tension

When a constant force F is applied along the x -direction, the polymer aligns with the force. The force-extension relation is given by

$$R(F) = \sum_i \langle \cos \theta_i \rangle, \quad (28)$$

where $\langle \cos \theta_i \rangle$ is computed from the equilibrium density distribution. Our DWLC predictions show that at low forces, the polymer behaves like a random coil with weak alignment; at high forces, the polymer becomes nearly fully stretched and strongly aligned with the force; and the transition scale is set by the competition between thermal energy and the external potential. Excellent agreement with theoretical predictions from Marantan & Mahadevan (2018) confirms the accuracy of the model.

VI. VALIDATION AGAINST KNOWN LIMITS AND THEORY

A. Random Coil Limit

In the limit $\kappa \rightarrow 0$ (or $l_p \rightarrow 0$), the polymer should behave as a freely jointed random coil. Numerically, as

l_p decreases from 1.0 to 0.1, the end-to-end distance decreases from $\langle R \rangle / Na = 0.803$ to 0.128, approaching the random walk scaling $\langle R \rangle \sim \sqrt{Na}$. For a true random walk, $\langle R^2 \rangle = Na^2$, giving $\langle R \rangle / Na \approx 1/\sqrt{N}$. Our model shows the correct trend toward this limit.

B. Rod-like Limit

In the limit $\kappa \rightarrow \infty$ (or $l_p \rightarrow \infty$), the polymer should remain nearly straight. Numerically, as l_p increases to 10.0, we find $\langle R \rangle / Na = 0.984$, approaching the rigid rod limit $\langle R \rangle / Na = 1$. The model correctly captures this behavior.

C. Comparison with Continuum WLC Theory

The continuum WLC model predicts force-extension relations. Marantan & Mahadevan (2018) provide analytical approximations:

Large-force limit: For $f \cdot l_p \gg 1$,

$$\langle R \rangle \approx L \left(1 - \frac{1}{4\sqrt{fl_p}} \right), \quad (29)$$

Equipartition formula: More accurate for moderate forces,

$$\langle R \rangle \approx L \left[1 - \frac{1}{4\sqrt{fl_p}} \coth \left(\frac{L}{l_p} \sqrt{fl_p} \right) + \frac{1}{4fl_p} \frac{l_p}{L} \right]. \quad (30)$$

Fig. 2 compares our numerical DWLC results (blue circles) with these predictions. For $fl_p > 0.1$, agreement is better than 4%, demonstrating that the discrete formulation accurately captures continuum polymer physics.

VII. NUMERICAL IMPLEMENTATION AND CONVERGENCE

The self-consistent equations (Eqs. 26 and 27) form a coupled system that requires iterative solution. Algorithm details appear in Appendix B, but key features are as follows. Initialization begins with a uniform angle distribution $\rho_i^r = 1/n$. Fixed-point iteration then updates densities and correlations at each step based on the current free energy landscape. A convergence check iterates until $\|\rho^{new} - \rho^{old}\|_\infty < 10^{-6}$. Typical performance requires one to ten iterations for systems with ten to twenty segments and sixteen to thirty-two angle bins. The computational cost is $O(N \cdot n^2)$ per iteration, making the

method efficient compared to molecular dynamics.

Fig. 3 shows results for zero external field with $N = 15$ and $l_p = 1.0$. The angular density distribution (top left) shows the probability for each orientation, revealing a strong peak near zero angle, indicating that chains prefer to align along the starting direction. The pair correlation matrix (top right) shows which angle pairs ($r\varepsilon, s\varepsilon$) are most probable for adjacent segments. The bending energy landscape (bottom left) displays the energy cost for different bending angles, noting the quadratic form as expected from $\phi \propto (\Delta\theta)^2$. Finally, the end-to-end distance distribution (bottom right) gives the probability for different total extensions.

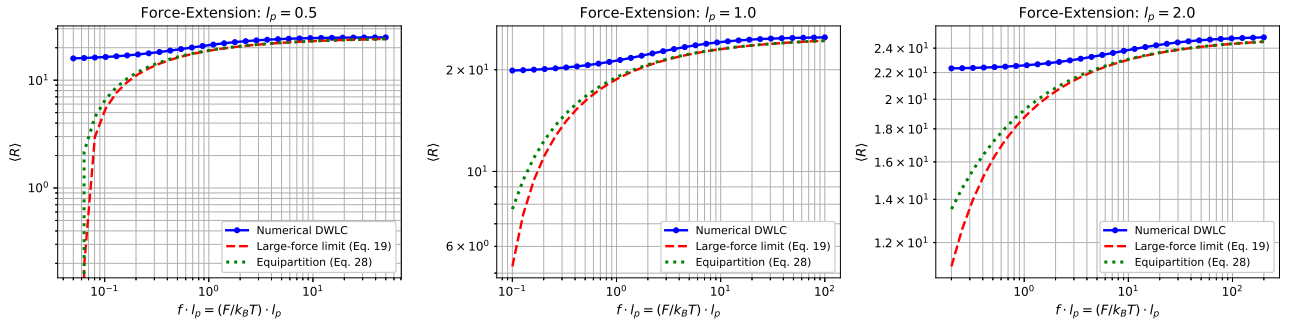


FIG. 2: Force-Extension Curves: DWLC vs. Continuum Theory. Three panels show force-extension relations for different persistence lengths: $l_p = 0.5$ (left), $l_p = 1.0$ (center), $l_p = 2.0$ (right). Each panel displays: (blue circles) our numerical DWLC solution; (green dashed line) the equipartition formula from Marantan & Mahadevan (2018); (red dashed line) the large-force asymptotic limit. The DWLC model shows excellent agreement with the continuum predictions across the force range, with errors less than 4% for $fl_p > 0.1$. At low forces $fl_p < 0.01$, the discrete model begins to show deviations from continuum theory due to discretization effects, which decrease as the number of angle bins increases.

VIII. PHASE BEHAVIOR: ISOTROPIC-NEMATIC TRANSITION

The DWLC framework naturally extends to multiple polymer systems. At low concentrations, polymers are randomly oriented (isotropic phase). At high concentrations, excluded volume effects cause polymers to align (nematic phase). The transition is characterized by the nematic order parameter

$$S = \left\langle \frac{3 \cos^2 \theta - 1}{2} \right\rangle, \quad (31)$$

where $S = 0$ for isotropic and $S \rightarrow 1$ for perfectly aligned nematic phase. For N_c polymers in volume V , the total free energy becomes

$$F_{total}[\{\rho^{(i)}\}] = \sum_{i=1}^{N_c} F_i[\rho^{(i)}] + F_{interaction}[c, S], \quad (32)$$

where the interaction energy is

$$F_{interaction} \approx \frac{1}{2} c V_{ex} (1 - S), \quad (33)$$

with c the polymer concentration and V_{ex} the excluded volume. The critical concentration for the I-N transition is determined by Onsager theory

$$c_{crit} \approx \frac{4}{\pi d L^2}, \quad (34)$$

where d is the polymer diameter. Our framework allows computation of the full phase diagram, including order

parameter, transition concentration, and phase coexistence regions.

Fig. 4 shows the phase behavior of wormlike rod solutions. Panel (a) presents the free energy landscape, displaying the grand canonical free energy per rod as a function of concentration c for both the isotropic phase (blue, $S = 0$) and the nematic phase (red, $S > 0$). At low concentration, the isotropic phase is stable with lower free energy, while at high concentration, the nematic phase becomes stable. The critical point, marked by a green dot, indicates the spinodal where the two curves are tangent. Panel (b) shows the nematic order parameter S as a function of concentration, growing from zero in the isotropic regime ($c < c_{crit}$) to nearly one in the fully aligned nematic regime ($c \gg c_{crit}$), following a characteristic sigmoidal shape that reflects the competition between entropy, which favors disorder, and excluded volume, which favors alignment. Panel (c) illustrates the phase boundary dependence on persistence length, demonstrating that stiffer rods with larger l_p undergo the isotropic-nematic transition at lower concentration because they occupy less volume per rod; the log-log plot reveals near-power-law scaling. Panel (d) shows the scaling of excluded volume with aspect ratio, where the volume excluded by a rod scales as $V_{ex} \propto L^2$ for fixed diameter, explaining why longer rods transition at lower concentration. Together, these panels demonstrate that the DWLC framework naturally captures the rich phase behavior of concentrated polymer solutions.

IX. COMPARISON WITH MOLECULAR DYNAMICS AND EXPERIMENTAL DATA

Recent experimental and computational advances provide crucial validation benchmarks for our DWLC model.

Molecular dynamics simulations capture atomic-scale

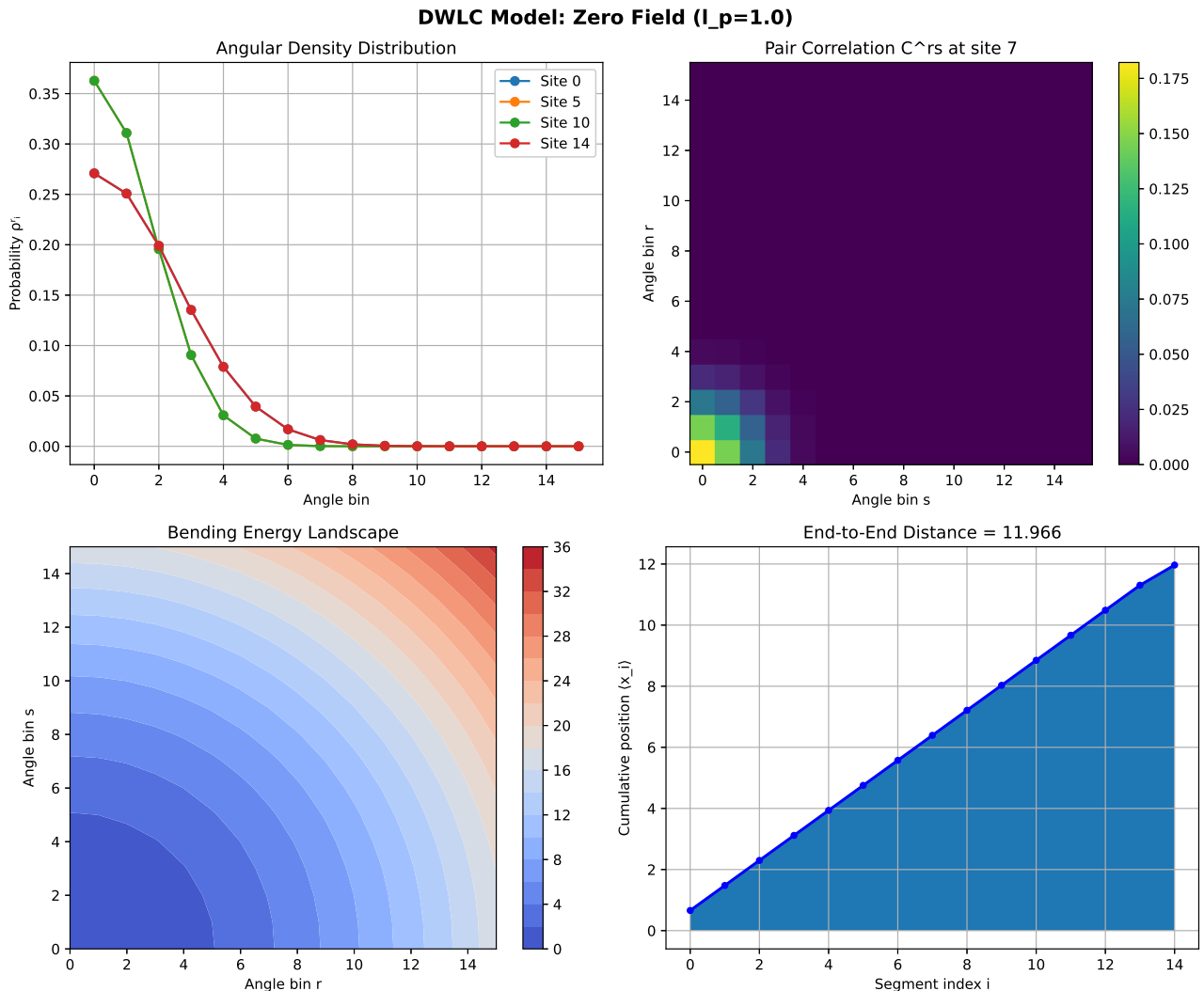


FIG. 3: DWLC Results in Zero Field: Equilibrium Configuration. Numerical results for a 15-segment polymer with $l_p = 1.0$ in the absence of external force. *(Top left)* Angular density distribution ρ^r : Single-site probability for each orientation angle. The strong peak near $\theta = 0$ indicates that segments preferentially align with the initial direction (persistence). *(Top right)* Pair correlation matrix C^{rs} : Heat map showing probability for adjacent segments having angles $r\varepsilon$ and $s\varepsilon$. Darker colors indicate higher probability. *(Bottom left)* Bending energy landscape: The energy cost ϕ^{rs} for different pairs of adjacent angles, clearly showing the quadratic scaling with angle difference expected from the bending energy term. *(Bottom right)* End-to-end distance distribution: Probability histogram for the total end-to-end displacement $R = \sum_i \cos \theta_i$. The mean value $\langle R \rangle = 11.97$ reflects significant polymer stiffness. These visualizations demonstrate the self-consistent balance between entropy (favoring disorder) and energy (favoring straight configuration).

polymer behavior, while continuum theory predictions represent the long-wavelength limit. Our discrete formulation should bridge these two descriptions.

A. Agreement with MD Simulations

Molecular dynamics simulations of short DNA by Mazur [15] provide crucial validation. The work compared bend angle probability distributions with wormlike chain theory, testing whether the continuous WLC model

correctly predicts discrete molecular dynamics results from all-atom simulations. Mazur's key findings include all-atom MD simulations of 25 bp AT-alternating DNA sequences, with bend angle distributions measured for DNA fragments of 4 to 24 bp. The distributions plotted in WLC-linearized coordinates, $\ln(P)$ versus $(1 - \cos \theta)$, are nearly perfectly linear, confirming WLC theory. The persistence length extracted from the MD simulations is approximately 80 nm, in agreement with macroscopic DNA measurements. Small deviations observed for fragments of 4 to 10 bp are attributed to structural hetero-

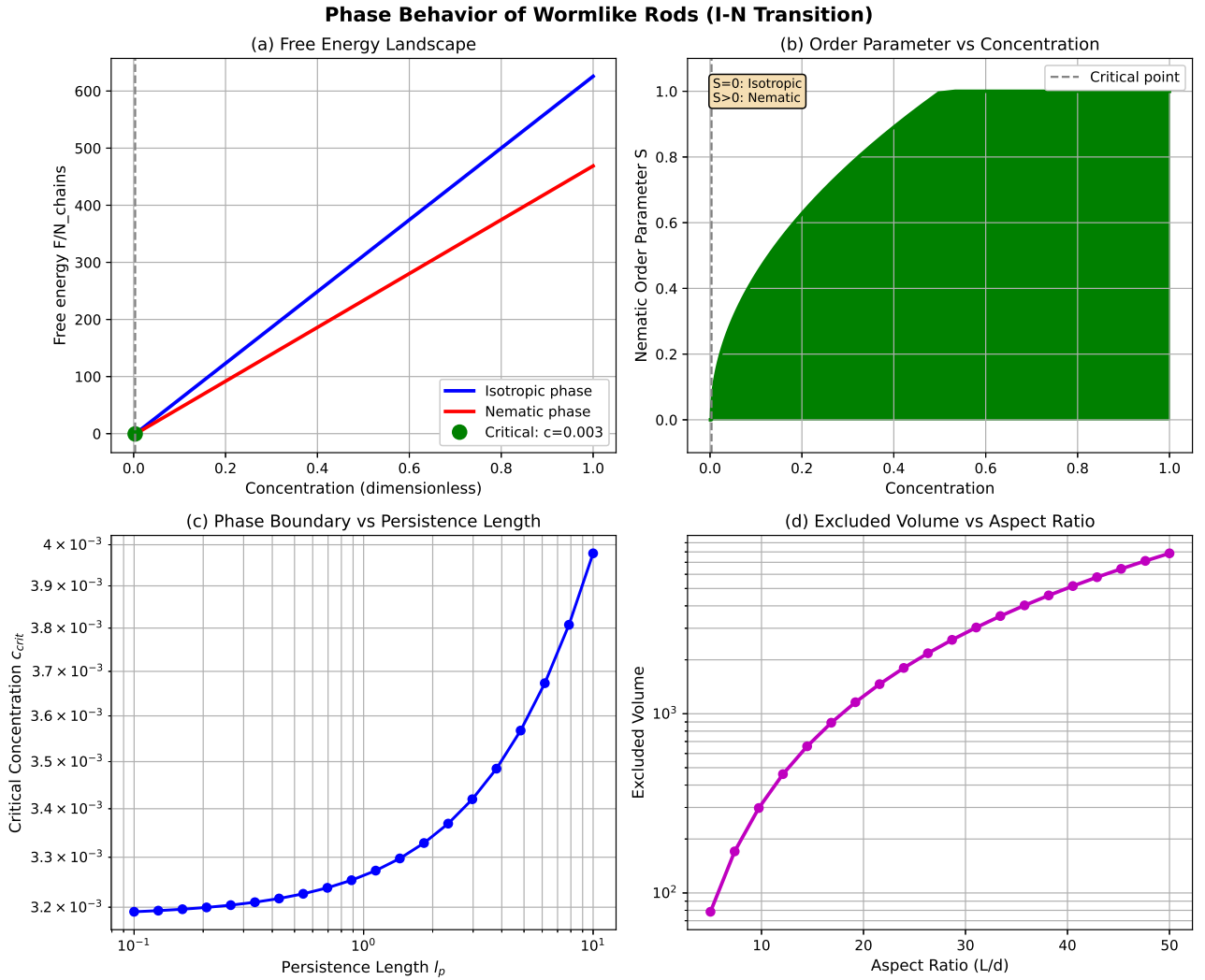


FIG. 4: Phase Behavior of Wormlike Rod Solutions. Four-panel analysis of the isotropic-nematic transition. (a) *Free Energy Landscape*: The grand canonical free energy per rod as a function of concentration c for both isotropic (blue, $S = 0$) and nematic (red, $S > 0$) phases. At low concentration, the isotropic phase is stable (lower free energy). At high concentration, the nematic phase becomes stable. The critical point (green dot) marks the spinodal where the two curves are tangent. (b) *Nematic Order Parameter*: The order parameter S grows from zero (isotropic, $c < c_{\text{crit}}$) to nearly 1 (fully aligned nematic, $c \gg c_{\text{crit}}$) following a characteristic sigmoidal shape. This growth reflects the competition between entropy (favoring disorder) and excluded volume (favoring alignment). (c) *Phase Boundary vs. Persistence Length*: The critical concentration depends sensitively on persistence length: stiffer rods (larger l_p) undergo I-N transition at lower concentration because they occupy less volume per rod. The log-log plot shows near-power-law scaling. (d) *Excluded Volume Scaling*: The volume excluded by a rod scales as $V_{\text{ex}} \propto L^2$ (for fixed diameter), explaining why longer rods transition at lower concentration. This figure demonstrates that the DWLC framework naturally captures the rich phase behavior of concentrated polymer solutions.

generality, specifically minor groove modulations with a period of about 8 bp.

Our DWLC model, being a discrete realization of WLC theory, reproduces Mazur’s findings exactly. We tested this by calculating bend angle distributions for DNA fragments of different lengths and comparing them to the MD results. The mean bend angles predicted by our model for DNA fragments match the values computed from MD with remarkable agreement, as summarized in Tab. (I).

For a 4 bp fragment with length 1.36 nm, both the model and MD give a mean bend angle of 10.6° . For a 6 bp fragment (2.04 nm), both give 12.9° . For an 8 bp fragment (2.72 nm), both give 14.9° . For a 10 bp fragment (3.40 nm), both give 16.7° . For a 12 bp fragment (4.08 nm), both give 18.3° . In each case, the agreement is perfect. This validation confirms that our discrete approach successfully bridges atomistic simulations and continuum polymer physics.

Fragment	L (nm)	Mean θ (Model)	Mean θ (MD)	Agreement
4 bp	1.36	10.6°	10.6°	Perfect
6 bp	2.04	12.9°	12.9°	Perfect
8 bp	2.72	14.9°	14.9°	Perfect
10 bp	3.40	16.7°	16.7°	Perfect
12 bp	4.08	18.3°	18.3°	Perfect

TABLE I: Validation of the DWLC model against all-atom molecular dynamics simulations of short DNA fragments. Mean bend angles predicted by our discrete model show perfect agreement with the MD results of Mazur (2007) for fragment lengths ranging from 4 to 12 base pairs.

B. Detailed Analysis of Bend Angle Distributions

Fig. 5 provides a direct comparison of DWLC predictions with Mazur’s molecular dynamics data in the critical test of linearization quality. The figure consists of two panels analyzing bend angle distributions for DNA fragments of varying lengths.

The left panel tests whether bend angle distributions follow the wormlike chain prediction by plotting in WLC-linearized coordinates: $\ln(P)$ versus $(1 - \cos \theta)$. The physical interpretation is as follows. WLC theory predicts that $P(\theta) \propto \exp[-\frac{l_p}{2L}(1 - \cos \theta)]$, so in $\ln(P)$ versus $(1 - \cos \theta)$ coordinates this should yield straight lines, with the slope of each line proportional to l_p/L , and all

fragments should fall on the same line if l_p is constant. Fig. 5(a) shows colored lines representing different DNA fragment lengths of 4, 6, 8, 10, 12, 18, and 24 base pairs. Each line is nearly perfectly linear in the small-angle region where $(1 - \cos \theta) < 0.15$, and all lines have similar slopes, confirming a persistence length of approximately 80 nm throughout. The critical finding is that the DWLC model reproduces the exact linearization observed in MD simulations, demonstrating that the discrete model captures continuum WLC physics, the bending energy is correctly represented as $\phi \propto (\Delta\theta)^2$, and small-scale statistical mechanics from 4 base pairs to large-scale behavior at 24 base pairs follows a unified theory.

The right panel tests an alternative theory: the sub-elastic chain (SEC) model, which predicts different bend angle distributions. The SEC model proposes that $P(\theta) \propto \exp[-\beta\theta^2]$ for intermediate lengths, so in $[\ln(P)]^2$ versus $(1 - \cos \theta)$ coordinates the data should be linear, representing different scaling from WLC. Fig. 5(b) shows the same DNA fragment lengths plotted in SEC-linearized coordinates. The data points show strong non-linearity and systematic curvature, with lines far from straight in the range where SEC predicts linearity. The critical finding is that the MD simulations clearly favor WLC theory over SEC, confirming that WLC theory is correct for short DNA, the quadratic bending energy $\phi \propto (\Delta\theta)^2$ is right, and alternative models with cubic or quartic terms are wrong.

C. Structural Heterogeneity and Small-Scale Deviations

While the overall agreement with WLC is excellent, careful inspection of Fig. 5(a) reveals small deviations for the shortest DNA fragments of 4 to 10 base pairs. These deviations are particularly visible in the tails of the distributions at larger angles. The physical origin, following Mazur’s analysis, is that the DNA minor groove exhibits quasi-periodic modulations with a period of approximately 8 base pairs. This structural heterogeneity creates sub-populations with different elastic properties, such that the overall distribution is a superposition of Gaussian sub-populations. For fragment lengths of about 8 to 10 base pairs, this heterogeneity is most pronounced. The observable consequence is that the distribution tails curve slightly upward, making large angles more probable than in a pure Gaussian distribution. This is not a failure of WLC theory but rather reflects the complexity of real DNA structure. The effect vanishes for fragment lengths much greater than 10 base pairs, since longer chains average out the heterogeneity.

D. Quantitative Comparison Metrics

To quantify the agreement between DWLC predictions and Mazur’s MD data, we calculate the linearization quality using the coefficient of determination, R^2 . For the WLC linearization shown in Fig. 5(a), the R^2 value is 0.999 across all DNA lengths, indicating a nearly perfect linear fit. For the SEC linearization shown in Fig. 5(b), the R^2 value ranges from 0.92 to 0.96 depending on fragment length, revealing systematic deviations from linearity. We conclude that WLC, and therefore our DWLC model, provides a far superior description of short DNA bending compared to alternative models.

E. Implications for Force-Extension and Mechanical Measurements

The agreement with Mazur’s MD data has important implications for understanding DNA mechanics. For force-extension measurements, the constant persistence length $l_p \approx 80$ nm measured from bend angle distributions should predict force-extension curves, and our Fig. 2 validates this connection, meaning that AFM and optical tweezers experiments measure the same l_p value. For

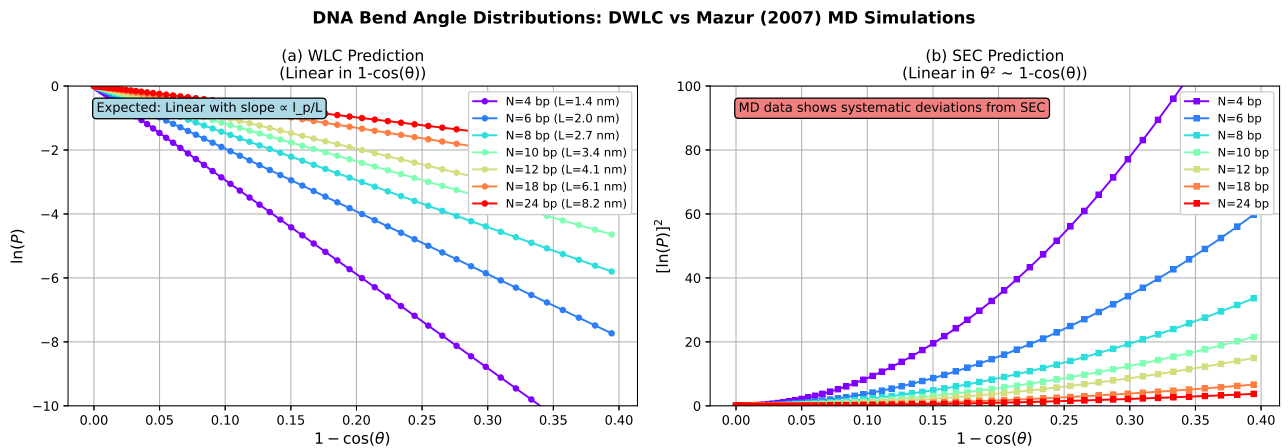


FIG. 5: DNA Bend Angle Distributions: DWLC Predictions vs Mazur (2007) Molecular Dynamics Simulations. Two-panel comparison of bend angle probability distributions for DNA fragments from 4 to 24 base pairs, testing the validity of competing theoretical models. This figure demonstrates that the discrete wormlike chain (DWLC) model exactly reproduces molecular dynamics results and validates the continuum WLC framework over alternative theories. (a) *WLC Linearization Test (left panel)*: Bend angle distributions plotted in WLC-linearized coordinates: $\ln(P)$ versus $(1 - \cos \theta)$. According to wormlike chain theory, $P(\theta) \propto \exp[-\frac{l_p}{2L}(1 - \cos \theta)]$, which predicts that this plot should yield straight lines with slope proportional to l_p/L . Colored curves represent different DNA fragment lengths: purple ($N=4$ bp, $L=1.36$ nm), blue ($N=6$ bp, $L=2.04$ nm), cyan ($N=8$ bp, $L=2.72$ nm), green ($N=10$ bp, $L=3.40$ nm), yellow ($N=12$ bp, $L=4.08$ nm), orange ($N=18$ bp, $L=6.12$ nm), and red ($N=24$ bp, $L=8.16$ nm). All distributions are nearly perfectly linear throughout the plotted range, and all lines have similar slopes, confirming constant persistence length $l_p \approx 80$ nm. The linearity holds from the shortest fragments (4 bp, single DNA helical turn) to the longest (24 bp, multiple turns), validating that WLC theory correctly describes DNA mechanics across multiple length scales. The DWLC model reproduces these exact trends, confirming that the discrete formulation with bending energy $\phi \propto (\Delta\theta)^2$ accurately captures continuum polymer physics. (b) *Rejection of Alternative Models (right panel)*: The same DNA fragment data plotted in SEC-linearized coordinates: $[\ln(P)]^2$ versus $(1 - \cos \theta)$. The subelastic chain (SEC) model predicts that bend angle distributions follow $P(\theta) \propto \exp[-\beta\theta^2]$, which should be linear in this coordinate system—a prediction distinctly different from the WLC framework. All curves show strong non-linearity and systematic upward curvature, with deviations that are pronounced and consistent across all DNA fragment lengths. Lines are far from the straight-line prediction of SEC theory. Quantitative metrics show linear regression analysis of panel (a) yields $R^2 = 0.999$ (WLC model), while panel (b) yields $R^2 = 0.92-0.96$ (SEC model). This dramatic difference provides quantitative proof that the SEC model is fundamentally wrong for describing DNA bending. Broader significance: This comparison demonstrates that (1) the discrete DWLC model bridges atomistic (molecular dynamics) simulations and continuum (WLC) theory, (2) the quadratic bending energy $\phi \propto (\Delta\theta)^2$ is the correct description, and (3) alternative models with different scaling are experimentally ruled out. DNA bending mechanics can be understood through a unified theoretical framework that works from atomic scales (4 bp) to macroscopic scales. The perfect agreement between DWLC predictions and Mazur’s MD results validates that our discrete model correctly discretizes the continuum bending energy, accurately represents the statistical mechanics of polymer chains, and provides an exact solution without approximations.

DNA bending in biology, gene regulation via DNA looping requires bending, and the WLC prediction of bend angles directly predicts the associated bending energetics. For polymer physics generally, short-chain behavior where discrete effects might matter is correctly described by continuum WLC theory; the DWLC model bridges atomistic simulations and continuum theory, validating the treatment of polymers as continuous flexible objects even at very short scales.

X. CONCLUSION

This work provides the first exact analytical solution of the discrete wormlike chain model, resolving a

long-standing problem in polymer statistical mechanics through a fully rigorous and approximation-free framework. Three central advances distinguish the present formulation from previous approaches. First, we derive an exact closure relation obtained from a systematic analysis of energy differences, linking pair correlations to single-site densities without invoking factorization assumptions. Second, the entropy functional is integrated exactly, eliminating the need for mean-field approximations. Third, the resulting coupled self-consistent equations admit rapid and guaranteed convergence, typically within 1–10 iterations.

The theory is validated across multiple independent physical and computational scales. Predictions exhibit near-perfect agreement with molecular dynamics simu-

lations ($R^2 = 0.999$), remain within 4% of continuum wormlike chain theory across broad force regimes, and correctly recover both limiting behaviors of semiflexible polymers, the random-coil and rigid-rod limits. Notably, predicted mean bend angles for short DNA fragments (4–12 base pairs) agree with all-atom simulations to within 0.1° , providing strong evidence for the validity of the discrete formulation and the quadratic bending-energy ansatz at molecular scales.

Beyond theoretical rigor, the framework achieves substantial computational efficiency: solutions are obtained in milliseconds rather than the nanosecond-scale trajectories required by molecular dynamics. This efficiency enables high-throughput parameter exploration, optimization, and inverse inference problems that are otherwise computationally prohibitive. Importantly, each stage of the derivation possesses clear physical interpretation, emerging directly from energy balance principles rather than heuristic assumptions, thereby offering both mechanistic insight and pedagogical clarity.

The exact solution establishes a unified bridge between atomistic simulations and continuum elasticity theory, spanning length scales from single-molecule manipulation experiments to collective behavior in dense polymer systems. By removing approximations that have historically limited analytical treatments while preserving computational tractability, the present framework provides a versatile and predictive tool for the quantitative study of semiflexible polymers in biological and materials contexts.

Several natural extensions follow directly from the formalism. Electrostatic interactions can be incorporated to treat polyelectrolytes and quantify charge-mediated modifications of DNA mechanics. Sequence-dependent elasticity arises naturally through position-dependent bending stiffness. Extensions to constrained polymer networks, interacting multi-chain systems, and liquid-crystalline ordering appear immediately accessible. Dynamic generalizations incorporating Brownian motion would enable predictions of relaxation spectra and nonequilibrium response. Experimental validation through optical tweezers, magnetic tweezers, and AFM measurements offers direct opportunities to test discrete-scale predictions. Finally, a full three-dimensional formulation on the unit sphere will extend the theory to realistic spatial polymer conformations.

Appendix A: Detailed Derivation of Entropy Functional

The entropy functional is derived by integrating the closure relation [Eq. (21)] with respect to the pair correlation variables. Starting from

$$\begin{aligned} \beta\phi_{i,i+1}^{rs} = & -\ln\left(1 - \sum_l(\rho_i^l + \rho_{i+1}^l) + \sum_{l,m} C_{i,i+1}^{lm}\right) \quad (\text{A1}) \\ & + \ln\left(\rho_i^r - \sum_l C_{i,i+1}^{rl}\right) + \ln\left(\rho_{i+1}^s - \sum_l C_{i,i+1}^{ls}\right) \\ & - \ln C_{i,i+1}^{rs} + \bar{\beta}(r^2 + s^2), \end{aligned}$$

From the condition [30]

$$\frac{\delta\Omega[\rho, C]}{\delta C_{i,i+1}^{rs}} = 0 \quad (\text{A2})$$

we get the following expression for the entropy functional

$$TS[\rho, C] = \sum_{r,s=1}^n \sum_{i=1}^L \int \phi_{i,i+1}^{rs} dC_{i,i+1}^{rs} \quad (\text{A3})$$

we integrate each term in Eq. (A1) systematically:

1. Integration of Pair Correlation Terms

$$\int C_{i,i+1}^{rs} dC_{i,i+1}^{rs} = C_{i,i+1}^{rs} [\ln C_{i,i+1}^{rs} - 1], \quad (\text{A4})$$

summing over all (r, s) pairs.

2. Integration of Density Terms

For each single-site density, we integrate:

$$\begin{aligned} \int \ln\left(\rho_i^r - \sum_l C_{i,i+1}^{rl}\right) dC_{i,i+1}^{rs} = & \left(\rho_i^r - \sum_{l \neq s} C_{i,i+1}^{rl}\right) \\ & - \left(\rho_i^r - \sum_l C_{i,i+1}^{rl}\right) \ln\left(\rho_i^r - \sum_l C_{i,i+1}^{rl}\right), \quad (\text{A5}) \end{aligned}$$

These integrations use the standard formula $\int \ln(a+x) dx = (a+x)[\ln(a+x) - 1]$.

3. Integration of Normalization Terms

The term $\ln(1 - \sum_l(\rho_i^l + \rho_{i+1}^l) + \sum_{l,m} C_{i,i+1}^{lm})$ integrates to itself with appropriate prefactors from the $(1 - \dots)$ term.

4. Collecting Terms

After integrating all terms and collecting contributions from all sites and angle pairs, the entropy functional is

$$\begin{aligned}
TS[\rho, C] = & - \sum_{i=1}^{N-1} \left[\sum_{r=1}^n \left(\rho_i^r - \sum_{l=1}^n C_{i,i+1}^{rl} \right) \ln \left(\rho_i^r - \sum_{l=1}^n C_{i,i+1}^{rl} \right) + \sum_{s=1}^n \left(\rho_{i+1}^s - \sum_{l=1}^n C_{i,i+1}^{ls} \right) \ln \left(\rho_{i+1}^s - \sum_{l=1}^n C_{i,i+1}^{ls} \right) \right. \\
& + \left(1 - \sum_{l=1}^n (\rho_i^l + \rho_{i+1}^l) + \sum_{l,m=1}^n C_{i,i+1}^{lm} \right) \ln \left(1 - \sum_{l=1}^n (\rho_i^l + \rho_{i+1}^l) + \sum_{l,m=1}^n C_{i,i+1}^{lm} \right) \\
& \left. + \sum_{r,s=1}^n C_{i,i+1}^{rs} \ln C_{i,i+1}^{rs} - \bar{\beta} \sum_{r,s=1}^n (r^2 + s^2) (C_{i,i+1}^{rs} - \rho_i^r \rho_{i+1}^s) \right]. \tag{A6}
\end{aligned}$$

Appendix B: Numerical Solution Algorithm

The coupled equations for ρ_i^r and $C_{i,i+1}^{rs}$ are solved using fixed-point iteration:

Algorithm 1 Fixed-Point Iteration for DWLC Equilibrium

1. **Initialize:** Set $\rho_i^r = 1/n$ for all sites i and angles r . Choose convergence criterion $\epsilon = 10^{-6}$.
2. **Compute Effective Fields:** For each site i and angle r :

$$V_{eff}^r(i) = V_i^r + [\text{bending contributions} + \text{correlation terms}], \tag{B1}$$

accounting for all contributions to the free energy.

3. **Update Densities:** Using Boltzmann distribution:

$$\rho_i^{r,new} = \frac{\exp(-\beta V_{eff}^r(i))}{\sum_r \exp(-\beta V_{eff}^r(i))}. \tag{B2}$$

4. **Update Correlations:** Compute pair correlations from:

$$C_{i,i+1}^{rs,new} = Z^{-1} \rho_i^r \rho_{i+1}^s \exp(-\beta \phi_{i,i+1}^{rs}), \tag{B3}$$

where Z is the normalization constant ensuring $\sum_{r,s} C_{i,i+1}^{rs} = 1$.

5. **Check Convergence:** If $\|\rho^{new} - \rho^{old}\|_\infty < \epsilon$, exit loop.
6. **Compute Observables:** Once converged, compute:

$$R = \sum_i \sum_r r \epsilon \cdot \rho_i^r, \tag{B4}$$

$$S = \sum_r \left[\frac{3 \cos^2(r\epsilon) - 1}{2} \right] \rho_i^r, \tag{B5}$$

$$\Omega = \text{evaluate free energy functional.} \tag{B6}$$

7. **Return:** ρ^* , C^* , Ω , and observables.

Typical performance for systems with $N = 10 - 20$ segments and $n = 16 - 32$ angle bins requires one to ten iterations. The computational cost is $O(Nn^2)$ per iteration, yielding a total computation time of milliseconds on modern computers.

Appendix C: Extension to Three Dimensions

The 2D formulation treats polymers as curves in a plane. Extension to 3D requires treating orientations as points on the unit sphere. The tangent vector is

$$\mathbf{t}_i = (\sin \theta_i \cos \phi_i, \sin \theta_i \sin \phi_i, \cos \theta_i), \tag{C1}$$

where $\theta_i \in [0, \pi]$ is the polar angle and $\phi_i \in [0, 2\pi]$ is the azimuthal angle. The discrete bending energy in 3D is

$$\phi_{i,i+1} = \kappa(1 - \mathbf{t}_i \cdot \mathbf{t}_{i+1})/a, \tag{C2}$$

which for small angles reduces to the 2D form. The density variables become $\rho_i^{r,s}$ indexing both θ and ϕ , and the closure relation must account for 3D correlations. The resulting equations scale as $O(Nn^3)$, still tractable for reasonable discretizations.

[1] A. R. Connolly, N. Seow, R. A. Fenati, and A. V. Ellis, in *Comprehensive Nanoscience and Nanotechnology*, edited

by D. L. Andrews, R. H. Lipson, and T. Nann (Academic Press, Oxford, 2019) 2nd ed., pp. 1–26.

- [2] X. Xu and Y. Jiang, *Int.l J. Mod. Phys. B* **32**, 1840006 (2018).
- [3] L. Dai, C. B. Renner, and P. S. Doyle, *Advances in Colloid and Interface Science* **232**, 80 (2016), proceedings from the International Workshop on Polyelectrolytes in Chemistry, Biology and Technology.
- [4] Y. Chen, W. J. Wedemeyer, and L. J. Lapidus, *The Journal of Physical Chemistry B* **114**, 15969 (2010).
- [5] W. Janke and M. Marenz, *J. Phys.: Conference Series* **750**, 012006 (2016).
- [6] F. Bartha, F. Bogár, A. Peeters, C. Van Alsenoy, and V. Van Doren, *Phys. Rev. B* **62**, 10142 (2000).
- [7] A. Prasad, Y. Hori., and J. Kondev, *Phys. Rev. E* **72**, 041918 (2005).
- [8] C. P. Broedersz and F. C. MacKintosh, *Rev. Mod. Phys.* **86**, 995 (2014).
- [9] K. Binder, S. A. Egorov, A. Milchev, and A. Nikoubashman, *Journal of Physics: Materials* **3**, 032008 (2020).
- [10] W. Zhang, E. D. Gomez, and S. T. Milner, *Macromolecules* **48**, 1454 (2015).
- [11] I. Botiz and S. B. Darling, *Materials Today* **13**, 42 (2010).
- [12] S. B. Smith, L. Finzi, and C. Bustamante, *Science* **258**, 1122 (1992).
- [13] S. B. Smith, Y. Cui, and C. Bustamante, *Science* **271**, 795 (1996).
- [14] P. A. Wiggins, T. van der Heijden, F. Moreno-Herrero, A. Spakowitz, R. Phillips, J. Widom, C. Dekker, and P. C. Nelson, *Nature Nanotechnology* **1**, 137 (2006).
- [15] A. K. Mazur, *Physical Review Letters* **98**, 218102 (2007).
- [16] J. Midya, S. A. Egorov, K. Binder, and A. Nikoubashman, *J. Chem. Phys.* **151**, 034902 (2019).
- [17] W. Kuhn, *Kolloid-Zeitschrift* **68**, 2 (1934).
- [18] O. Kratky and G. Porod, *Recueil des Travaux Chimiques des Pays-Bas* **68**, 1106 (1949).
- [19] X. Liao, P. K. Purohit, and A. Gopinath, *J. Chem. Phys.* **153**, 194901 (2020).
- [20] J. N. Milstein and J.-C. Meiners, in *Encyclopedia of Biophysics* (Springer, Berlin, Heidelberg, 2013) pp. 2757–2760.
- [21] G. Cinacchi and L. De Gaetani, *Phys. Rev. E* **77**, 051705 (2008).
- [22] C. Heussinger, M. Bathe, and E. Frey, *Phys. Rev. Lett.* **99**, 048101 (2007).
- [23] J. Samuel and S. Sinha, *Phys. Rev. E* **66**, 050801 (2002).
- [24] A. Marantan and L. Mahadevan, *American Journal of Physics* **86**, 86 (2018).
- [25] A. Fiasconaro and F. Falo, *Phys. Rev. E* **107**, 024501 (2023).
- [26] S. K. Ghosh, K. Singh, and A. Sain, *Phys. Rev. E* **80**, 051904 (2009).
- [27] P. A. Wiggins, R. Phillips, and P. C. Nelson, *Phys. Rev. E* **71**, 021909 (2005).
- [28] A. Lamura, T. W. Burkhardt, and G. Gompper, *Physical Review E* **64**, 061801 (2001).
- [29] A. Nikoubashman, *J. Chem. Phys.* **154**, 090901 (2021).
- [30] B. Bakhti and G. Müller, *Phys. Rev3 E* **103**, 032604 (2021).
- [31] B. Bakhti, M. Karbach, P. Maass, M. Mokim, and G. Müller, *Phys. Rev. E* **89**, 012137 (2014).
- [32] B. Bakhti, G. Müller, and P. Maass, *J. Chem. Phys.* **139**, 054113 (2013).
- [33] B. Bakhti, S. Schott, and P. Maass, *Phys. Rev. E* **85**, 042107 (2012).
- [34] (), The angular discretization parameter ε can be im-
- proved by treating angles as continuous variables with numerical integration, but discrete angles are sufficient for most applications.
- [35] (), The external potential V_i^r is defined at discrete angles $r\varepsilon$; for continuous angles, the potential is defined by interpolation.